

Achieving Highly Anisotropic Three-Dimensional, Lightweight, and Versatile Conductive Wood-Graphene Composite

Li Wang

Inner Mongolia University of Science & Technology

Xiao Tao Zhang

Inner Mongolia Agricultural University

Xi Ming Wang

Inner Mongolia Agricultural University

Zhang Jing Chen

Virginia Polytechnic Institute and State University

Yu Kun Ren

Sanofi Global R&D

Sun Guo Wang

Sungro Bioresource & Bioenergy Technologies Corp

Zhe Wang

Inner Mongolia Agricultural University

Li Li Li

Inner Mongolia Agricultural University

Jian Fang Yu (✉ yjf_112@163.com)

Inner Mongolia Agricultural University

Qin He

Inner Mongolia Agricultural University

Li Hong Yao

Inner Mongolia Agricultural University

Yi Nan Hao

Inner Mongolia Agricultural University

Li Jun Ding

Inner Mongolia Agricultural University

Qi Li

Inner Mongolia Agricultural University

Hua Qiong Duo

Inner Mongolia Agricultural University

Marshall WHITE

Research Article

Keywords: Conductivity, Conductive wood, Volume resistivity, Three-dimensional anisotropic, Lightweight

Posted Date: June 22nd, 2021

DOI: <https://doi.org/10.21203/rs.3.rs-602232/v1>

License:  This work is licensed under a Creative Commons Attribution 4.0 International License.

[Read Full License](#)

Abstract

Functionality of wood has to evolve with time to adapt to the emerging needs in society. In this work, endowing electrical conductivity to the insulating wood by adding graphene into the wood matrix to form a conductive wood-graphene composite (conductive wood) via a facile and environmentally benign fabrication technique. The rationale of fabricating conductive wood is of two folds: (1) The high suitability of wood as a renewable matrix due to its porous network and mechanically robust monolithic structure. (2) The need to explore reasonable strategy to adequately translate the properties of graphene from microscopic level to macroscopic level. The conductive wood is able to preserve both the natural features of wood (to function as mechanical scaffold) and the conductivity of graphene. An outstanding electrical conductivity (volume resistivity of $36.7 \Omega \cdot \text{cm}$) is achieved for the conductive wood, while it can maintain a low bulk density of 0.44 g cm^{-3} . More significantly, the conductive wood demonstrates a highly three-dimensional anisotropic conductivity that makes it a highly versatile conductor in various applications. Hence, this lightweight conductive wood may contribute towards a great electronic revolution and as an encouraging strategy to repurpose the function of wood in this new era.

Introduction

Since the dawn of time, wood has been used in structural applications due to its highly renewable nature and its excellent mechanical properties[1, 2]. Even though wood is still prized as one of the essential building materials in this era, its revered status is slowly eroded by the development of mechanically robust structural materials such as steel. As such, functionality of wood has to evolve to adapt to the emerging demand in our society. In particular, electrical conductor has become one of the essential materials in this current technologically developed society due to the increasing need for electronics. However, as a result of the electrical insulating behavior of wood (conductivity of $10^{16} \Omega \cdot \text{cm}$)[3], it is less intuitive to employ wood as electrical conductor as compared to the more matured semiconducting materials such as Si, Ge, and GaAs. Despite this apparent flaw, the concept of utilizing wood to replace the non-renewable elements used in conducting application remains to be exciting due to its high abundance and renewable nature. Furthermore, the typically conductors/semiconductors possess high densities which makes it highly unsuitable for weight-sensitive application. Hence, it is highly desirable to achieve electrically conductive wood which can potentially address the rising need in electronic devices and to reduce the demand of the non-renewable conductors.

The most prevalent strategy to confer new properties to material is through the fabrication of composite[4]. Such strategy is especially suitable for wood as it is a porous material with high density of oxygen functionalities, *e.g.* carboxylic acid and hydroxyl groups, which allows the incorporation of filler material into the wood matrix[5]. As such, wood is a fascinating material that has received significant research interest in recent years, whereby several techniques such as drop-casting, carbonization, and CO_2 laser scribing process[6-14] have been attempted so as to improve its electrical conductivity. Even though these strategies have generally resulted in the fabrication of electrically conductive wood-based products, these techniques often result in considerable coating spalling, non-uniform distribution of

conductive fillers, or a significant increase in the density of the composite. In addition, these techniques usually consume large amount of energy which indirectly increases the cost and intensifies the pollution concerns[15-17]. Furthermore, some of these methods such as CO₂ laser scribing process may consider to be technologically sophisticated for efficient large-scale production[10, 11]. As such, identification of suitable conductive material, and fabrication strategy are some of the vital factors in realizing functional conductive wood composite.

Graphene is a two-dimensional material with single-layer carbon atoms bonded into a honeycomb lattice. It has been widely studied in numerous applications such as energy storage devices[18, 19], thermal conductors[20], drug delivery[21-23], and etc. Owing to its electrons being able to move through the graphene lattice like a massless Dirac fermion[24, 25], graphene possesses excellent electrical conductivity which makes it highly appealing in electrical conducting application. Furthermore, its lightweight property is particularly attractive in achieving low density electrical conductor which may be important for weight-sensitive applications[26-28]. While graphene is able to demonstrate marvelous properties in the microscopic level, effective translation of its properties from the microscopic level to the macroscopic level is highly desired to realize functional products. Even though graphene monoliths as graphene paper[29, 30] and graphene aerogel[31, 32] have been introduced as three-dimensional conductors, these materials are unable to exhibit anisotropic behavior which limits its versatility. Recently, there have been demonstrations of incorporating graphene into the wood in an attempt to fabricate conductive wood-graphene composite[12, 33]. Despite the successful demonstration of these wood-graphene composite, the tendency of graphene sheets restacking could potentially reduce the overall conductivity[34]. Hence, realizing an efficient graphene-wood composite with enhanced electrical conductivity remains to be a challenge.

In this work, the graphene is introduced into a poplar wood via a simple vacuum pressure impregnation process, with subsequent reduction using a green reducing agent, *i.e.* ascorbic acid. Interestingly, the cross-section of the conductive wood has the lowest resistivity of *ca.* 36.7 Ω·cm among all three orientations (591.4 Ω·cm for radial section, and 3231.3 Ω·cm for tangential section), which suggests that the conductive wood is able to exhibit anisotropic electrical conduction property. In addition to the anisotropic electrical conductivity, the conductive wood is able to retain its low density of 0.44 g cm⁻³ (close to that of the natural wood *ca.* 0.43 g cm⁻³), which is highly suitable for weight-sensitive applications. Thus, based on these promising results, it is expected that this lightweight conductive wood proposed in this work can potentially become a highly versatile conductor that can tailor to various applications.

The preparation of conductive wood is illustrated in **Figure 1**. In brief, wood is firstly retrieved from a poplar trunk into the dimensions of 30 mm × 30 mm × 10 mm, and then it is subsequently dehydrated for extractive and sawdust accumulated during wood processing and transportation. After which, the dehydrated wood is mixed with GO and the GO/wood mixture undergoes a pulsed vacuum for 15 min. After drying the sample at 60 °C for 24 h, ascorbic acid (AA) is added to reduce GO/wood composite (100

°C for 2 h) to obtain the final sample rGO-wood, denoted as conductive wood. The sample is dried in a vacuum oven at 60 °C for 24 h to ensure that the moisture content in the sample is less than 10 %. The dried sample is then used as conductive wood. An illustration of the bonding and conduction mechanism for conductive wood is proposed in **Figure 1g-i**. **Figure 1g** shows the illustration of the aligned structure of the conductive wood. The resistivity of the material is determined using the Hall effect method which can directly shows the carrier concentration and mobility of the material as shown in **Figure 1k**. It illustrates that there is a complete conductive path in the conductive wood which facilitate the passage of electrons. This method is can also determine the Hall coefficient of the material which indicates that the material exhibits Hall effect. As a demonstration, the conductive wood is able to light up a LED bulb when connected to an external power source, as shown in **Figure 1l**.

Results And Discussion

In order to achieve a successful fabrication of a conductive wood composite, it is necessary to first prepare GO fillers with reasonable chemical and physical properties. In this work, GO is prepared from various graphite meshes (more details in Supporting Information, **Figure S1**). It is shown that GO prepared from 4000 mesh graphite is able to demonstrate a uniform lateral size of *ca.* 1-2 μm . This uniform size of 1-2 μm for GO is crucial in this work in order to avoid clogging the wood vessels. Atomic force microscopy (AFM) is conducted to investigate the as-synthesized GO in terms of thickness, and the result is shown in **Figure 2a**. Based on the AFM topographic map, it can be observed that the lateral size of GO is *ca.* 2 μm which is in good agreement with the SEM image (**Figure S1d**) and the size distribution chart (**Figure S1f**). Furthermore, it is observed from the topographic map that the GO sheets are uniform in size with a consistent thickness across the various GO sheets. According to the height profile shown in **Figure 2b**, similar observation can be made regarding the uniform lateral size and uniform height of different GO sheets. The thickness of GO is *ca.* 1.23 nm, which is a close approximation to the single-layer GO. Thus, based on the results, it is suggested that the as-synthesized GO is likely to possess a single-layer or few-layer configuration, which is highly suitable to be impregnated into the wood vessels. Furthermore, such single-layer or few-layer configuration can further enhance the electrical conductivity due to the lower interfacial resistance that can arise during GO restacking. X-ray photoelectron spectroscopy (XPS) is conducted on the as-synthesized GO, as shown in **Figure 2c** and **2d**. **Figure 2c** shows the high-resolution C1s spectrum of GO. Based on the deconvolution, the three main peaks can be identified, namely at 284.6 eV (C-C/C=C), 287 eV (C-O), and 288.6 eV (O-C=O). This result indicates that there is a higher density of hydroxyl group (-OH) presented in GO which is available for hydrogen bonding to the cellulose in the wood vessel. **Fig. 2d** shows the high-resolution O1s spectrum of GO. It can be observed that a large peak (in terms of area) belongs to C-O at 532.8 eV, which is in good agreement with the C1s spectrum. Thus, based on the SEM, AFM, and XPS results for GO, it can be concluded that the as-synthesized GO is highly suitable as a filler in wood due to its uniform size distribution, 1-2 μm lateral size, and abundant -OH functional group which allows efficient infiltration and effective hydrogen bonding onto the wood vessel.

The surface morphologies and EDS analysis of natural wood, GO/wood and conductive wood are presented in **Figure 3**. The natural wood, shown in **Figure 3a**, is infiltrated with GO to form GO/wood (**Figure 3b**) composite after a series of optimization (more details in Supporting Information, **Figure S2**). It can be clearly observed that the color of the natural wood changed to brown after processing the wood with GO, which hints the successful incorporation of GO into the natural wood. After which, GO/wood composite is reduced with the use of a mild reducing agent, *i.e.* ascorbic acid, to form the final rGO/wood (denoted as conductive wood) as shown in **Figure 3c**. The conversion of the brown GO/wood to black metallic conductive wood suggests the successful reduction of GO to rGO within the wood. Thus, based on the color change, it is indicative of the successful GO infiltration into the wood and its subsequent reduction to rGO. In order to investigate the morphologies of the various wood samples at the microscopic level, scanning electron microscope (SEM) is employed. The cross-section orientation of various wood samples is firstly investigated. Based on **Figure 3d, 3e, and 3f**, it can be observed that the pores in the natural wood (**Figure 3d**) gradually becomes smaller when GO is added (**Figure 3e**) and after reducing the GO (**Figure 3f**). Higher magnification SEM of the cross-section orientation of three wood samples are presented in **Figure S3**. The radial section of the wood is also investigated as shown in **Figure 3g, 3h, and 3i**. It can be observed that the open spaces within the wood cells are filled after the addition of GO. This result exhibits the uniform distribution of rGO in the internal wall of the pore and therefore resulting in a unique rGO/wood structure with a tightly intertwined rGO/cell wall configuration. Higher magnification of the radial section of the wood is shown in **Figure 3j, 3k, and 3l**. It can be observed that the pores of the natural wood (**Figure 3j**) that are initially visible gradually becomes smaller after the addition of GO. This result may suggest that the shrinkage in the pores could be due to the wrapping of GO around the internal wall of the pores. Elemental dispersive spectroscopy (EDS) analysis of different samples is performed to confirm the degree of reduction of GO in the wood samples and the results are presented in **Figure 3m, 3n, and 3o**. For the natural wood, it has a C/O ratio of 2.30 (**Figure 3m**), and after adding GO the C/O ratio is reduced to 0.95 (**Figure 3n**). This could be explained by the addition of GO with abundant oxygen moieties into the system. After reducing the GO/wood, the C/O ratio increases to 3.60 (**Figure 3o**) which is indicative of a successful reduction of GO to rGO by AA. As such, rGO would be able to facilitate the effective conduction of electricity in the conductive wood.

In order to investigate the bonding between graphene and wood, a series of characterization techniques are employed. XPS is firstly used to study the species in the natural and modified wood, and their survey scans are shown in **Figure S4**. The high-resolution C1s XPS spectrum of natural wood in **Figure 4a** reveals four obvious peaks located at 289.2 eV (O-C=O), 288.1 eV (C=O/C-O-C), 286.5 eV (C-O), and 284.8 eV (C-C). In particular, there is a high content of C-O bonding in the natural wood which decreases after the formation of rGO/wood (**Figure 4b**). Such a decrease in C-O bonding could indicate that -OH is used for the hydrogen bonding between GO and the cellulose of the wood vessels. The O1s XPS spectra of natural wood (**Figure 4c**) and conductive wood (**Figure 4d**) present similar results to the C1s XPS spectra (**Figure 4a and 4b**), as both peaks at 533.1 eV (O-C=O) and 531.1 eV (C-O) show a decrease for the conductive wood. The decrease in the C-O content in the conductive wood could be due to the formation of hydrogen bonding between wood and GO, which provides effective GO adhesion around the internal

wall of the pore that is observed in the SEM images (**Figure 3f, 3i, and 3l**). The slight decrease in the other oxygen functionalities in the conductive wood could be due to the reduction by AA. In order to further verify the bonding between wood and GO, Fourier transformed infrared (FTIR) spectra of natural wood and conductive wood are shown in **Figure 4e**. The results show that both FTIR spectra of the natural wood and conductive wood are fairly similar which indicates that there are subtle chemical changes within the wavenumber of 500 to 2000 cm^{-1} . Interestingly, it can be observed that the peak located at 3370 cm^{-1} , which can be attributed to the -OH stretching vibration, is significantly larger for conductive wood as compared to natural wood. The deviation of wavenumber to a lower position around 3500 cm^{-1} indicates the formation of hydrogen bonding between the oxygen functionalities in GO and in cellulose, which led to the alteration of the absorbance of -OH stretching vibration[36-39]. This implies that GO is bonded to the wood vessels via hydrogen bonding by either forming -OH to -OH or -OH to -O-bonding[33]. In addition, the slight increase in the 608 cm^{-1} peak for conductive wood compared to natural wood may suggest the presence of π - π stacking between the GO and the wood[40], which can contribute towards the bonding of graphene onto wood. Thus, based on the FTIR results, it can be concluded that hydrogen bonding is most likely to the main bonding mechanism between wood and GO, which is consistent with the XPS results shown earlier (**Figure 4a and 4b**).

Figure 4f shows the X-ray diffraction (XRD) spectrum of natural wood shows three characteristic peaks for cellulose at 17° (101), 23° (002), and 37.5° (040)[41]. The change in the crystallinity of the wood is reflected by the change in the (002) diffraction peak, since (002) is directly related to the wood crystallinity. For GO/wood and rGO/wood, the position of the crystalline peak, *i.e.* 23°, remains the same. This indicates that the addition of GO and the subsequent reduction process by AA do not influence the crystallinity of the wood, and the original physical structure of wood is still preserved. This is shown from the estimation based on diffraction intensity of the peak at 22°, whereby it is determined that the crystallinity of natural wood is *ca.* 48%, while the crystallinity of conductive wood is *ca.* 50%. However, the diffraction peaks at $2\theta=16.1^\circ$ and 22.2° are weakened due to the hydrogen bonding between rGO and the internal structure in wood. The diffraction peak at $2\theta=29.0^\circ$ is the characteristic diffraction peaks of graphite-like compounds (002). The crystallographic plane (001) and (100) distinct peaks of GO at diffraction angles of 9.42° and 43.0° are weakened, which can be attributed to the formation of rGO in the pores of the wood.

The thermogravimetric analysis (TGA) and differential thermogravimetry (DSC) curves of the natural wood and conductive wood are shown in **Figure S5a and S5b**. In the temperature region of 50 °C to 150 °C, the mass loss can be attributed to the evaporation of the adsorbed moisture in the wood (*ca.* 4% mass loss). In the second temperature region of 150 °C to 350 °C, the mass loss is related to the initial oxidative decomposition of the wood components which is mainly due to the degradation of hemicellulose followed by cellulose and lignin (*ca.* 62% mass loss) degradation. Finally, the third temperature region (above 350 °C) presents the char oxidation of wood (*ca.* 34% mass loss)[42]. According to **Figure S5a**, the conductive wood is less sensitive to heat than the natural wood. This is probably due to the high density of hydrogen bonding between the wood and rGO. Based on **Figure S5b**, it

can be observed that the conductive wood is firstly endothermic and then exothermic with the increase in temperature from room temperature to 100 °C. When temperature is less than 100 °C, the exothermic peak of the natural wood is smaller as compared to conductive wood which is due to the breaking of hydrogen bonding between the free water molecules and the hydroxyl groups. This means that there are fewer free hydroxyl in the conductive wood available to bond with the water molecules. This could be due to the utilization of the hydroxyl group in wood to form hydrogen bonding with the graphene. As the temperature increases to 255 °C, there is a large weight loss for the natural wood with a corresponding exothermic peak produced in the DSC curve, which could be due to the degradation of hemicellulose and cellulose in wood (**Figure S5b**). This result indicates that rGO in conductive wood is bonded to the free hydroxyl groups in hemi-cellulose and cellulose which results in the weakening of their extent of degradation. When temperature increases to 371 °C, this is the temperature at which cellulose degrades[43]. The exothermic peak of the natural wood is larger as compared to conductive wood, which further illustrates the hydrogen bonding between rGO and cellulose. An exothermic peak appears at 466 °C for the natural wood, while a smaller exothermic peak appears at 499 °C for conductive wood. This stage can be attributed to the degradation of lignin[44]. Due to the π - π stacking between rGO and the aromatic ring of lignin, the degradation temperature of lignin becomes higher in conductive wood as compared to natural wood. Therefore, based on the above analysis, rGO can aid in the enhancement of the thermal stability of wood due to the interaction with the three major components in the wood.

In order to understand the conduction mechanism, pore structures of natural wood and conductive wood are investigated using a mercury intrusion method and N₂ adsorption/desorption isotherm. **Figure 5a** shows the cumulative intrusion of both natural and conductive wood. It can be observed from **Figure 5b** that there is a bimodal pore distribution for conductive wood whereby the diameters of the pores in conductive wood are mainly within 90092-10659 nm and 1593-756 nm. This could be attributed to the continuous covalent network structure of rGO that is mainly deposited and bonded with the micropores and partial mesopores and macropores[45]. To further study the pore structure of conductive wood, N₂ adsorption-desorption isotherms of natural wood and conductive wood are conducted. **Figure 5c** shows that the conductive wood exhibits a lower quantity adsorbed/desorbed at various pressure regions as compared to natural wood. This indicates that the pressure range for capillary condensation to occur is smaller than the natural wood. The pore size distribution, shown in **Figure 5d**, reveals a higher quantity of smaller mesopores in the conductive wood (pore size *ca.* 15 nm) as compared to the natural wood (pore size *ca.* 30 nm). This reduction in the pore size for conductive wood could be due to the wrapping of graphene around the internal wall of the pores, and hence causing the shrinkage in the pore size. Thus, based on the collective results, due to the single-layer or few-layer configuration of the synthesized GO, and the slight decrease in the pore size in conductive wood, it is expected that the GO restacking issue in the conductive wood is almost negligible. As the conductive wood still retains a porous nature, it has a low bulk density of 0.44 g cm⁻³ which is highly suitable for weight-sensitive applications since most of the known conductors/semiconductors have high densities (*e.g.* Al has a density of 2.7 g cm⁻³, Cu has a

density of 8.96 g cm^{-3} , Si has a density of 2.3 g cm^{-3}). A table summarizing the pore structure of natural wood and conductive wood is shown in **Table S1**.

Three-dimensional Anisotropic Electrical Conductivity

The conductive wood is then tested for its electrical conductivity. A one-dimensional series conductive path was built by the conductive wood as shown in **Fig 6a-c**. With the switch turned on, a LED bulb was lighted up, and the corresponding voltage values were displayed as cross-section (18.3v), radial-section (28.4v), and tangential-section (31.7v), respectively, when using a current of 3.00 amp. Moreover, from **Fig 6d**, it can be demonstrated that a three-dimensional anisotropic electrical conductivity property, whereby there are distinct measured resistivities went through the cross-section, radial-section, and tangential-section of conductive wood. This is, to the best of our knowledge, the first demonstration of a distinct anisotropic electrical conductivity across three different orientations. Using the Van der Pauw method, various parameters such as resistivity, carrier density, carrier type and concentration, and Hall coefficient of the samples can be calculated[46]. **Video S1** shows the demonstration of conductive effect in 3D directions of conductive wood (recorded by high speed camera), and **Fig 6a-c** show the circuit effect images of conductive wood in three directions (cross-section, radial-section and tangential-section, respectively) from **Video S1**. The sample was fixed in the closed-loop conducting circuit before each test, and the switch then turned on, a LED was illuminated, when the brightness of the LED is the same, different voltage values are displayed in three directions. As shown in **Table S2**, the cross-section of the conductive wood has the lowest resistivity of *ca.* $36.7 \Omega \cdot \text{cm}$ among all three orientations ($591.4 \Omega \cdot \text{cm}$ for radial-section, and $3231.3 \Omega \cdot \text{cm}$ for tangential-section). This is largely due to the high amount of carrier concentration of $6.86 \times 10^{13} \text{ vm}^4$ along the cross-section as compared to the other two orientations. Furthermore, the cross-section orientation exhibits the highest Hall coefficient without a magnetic field. Laser confocal Raman microscopy (CRM) is used to investigate the chemical composition of the sample. **Figure 6e** and **6f** both reflect the distribution and different reduction degrees of rGO in a unit area by “D” and “G” peak variation, which represents the rGO connected in wood pores[47]. **Figure 6e** shows a random selection of conductive wood $20 \mu\text{m} \times 20 \mu\text{m}$ “G” peak distribution area, it can be seen that the continuity of the “G” peak is very good, indicating that the distribution of rGO is continuous, which helps to form a conductive path[48]. Moreover, **Figure 6f** showed the whole CRM spectrogram of conductive wood. According to **Figure 6f**, the distribution of a stronger “G” peak corresponds to the random region in **Fig 6e**. It can be concluded from **Fig 6e** and **6f** that the GO is well reduced by AA to achieve rGO, and it is uniformly dispersed across the wood. Thus, this three-dimensional anisotropic electrical conduction behavior of the conductive wood in this work could be a highly versatile conductor for various applications. Such fabrication method could have some advantages to the previously reported wood with enhanced conductivity as shown in **Table S3**. Furthermore, an ideal high-speed electronic with low-energy-consumption[49,50] could be realized using this three-dimensional anisotropic conductive wood, which may renew the age of electronics[51,52].

Conclusion

In this work, wood with anisotropic conductivity is formed by the hydrogen bonding of GO to the cellulose of the wood vessel, followed by its subsequent chemical reduction with the use of AA. The prepared sample exhibits a surface resistivity and volume resistivity of $120.0 \Omega \cdot \text{cm}$ and $36.7 \Omega \cdot \text{cm}$, respectively. With the use of a series of characterization techniques, it can be confirmed that GO is hydrogen bonding to wood due to the availability of oxygen functionalities. Furthermore, it is also shown that GO has been reduced to rGO which was distributed uniformly in the conductive wood. More importantly, the increasing order of volume resistivity conductivity values in three directions of conductive wood is cross-section>radial-section>tangential-section. This result demonstrates the distinctive anisotropic electrical conductivity of the fabricated wood. It is worth noting that the conductive wood maintains a relatively low density of 0.44 g cm^{-3} which could potentially make it highly appealing in weight-sensitive applications. Thus, with the exceptional three-dimensional anisotropic conductivity, this lightweight conductive wood could be an ideal low-energy-consumption and high-speed electronic device, which can expand the practical and efficient application field of wood as semiconductor materials and may bring a great electronic revolution in future.

Materials And Methods

Poplar. 11 years, is selected from a fast-growing poplar plantation. Straight-grained sapwood boards of fast-growing poplar wood with 151% initial moisture content are obtained from Hohhot, Inner Mongolia Autonomous Region, China. The wood is cut into 3 cm thick plain-sawed lumbers and then transported to the laboratory.

Statement: We confirm that all methods were performed in accordance with the relevant guidelines and regulations. And we ensure that we have obtained permissions to collect Poplar.

Chemical agents. Graphite powder (99.95% metals basis, 8000 meshes), potassium permanganate (KMnO_4 , 99.0%), sulfuric acid (H_2SO_4 , 98.0%), hydrochloric acid (HCl , 38.0%), hydrogen peroxide (H_2O_2 , 30.0%), sodium nitrate (NaNO_3 , 99.0%), silver nitrate (AgNO_3 , 99.5%), Barium chloride (BaCl_2 , 98.5%), Ascorbic acid (AA, $\text{C}_6\text{H}_8\text{O}_6$), and ethanol (98.5%) are acquired from Aladdin Industrial Corporation and they are used without any further purification.

Synthesis of Graphene Oxide (GO). 2.0 g graphite and 2.0 g NaNO_3 are added to 92 mL sulfuric acid (98%) and stirred for 3 h at 5°C in a round-bottomed flask. After which, 12.0 g KMnO_4 is added dropwise, blended, and stirred for 0.5 h. The samples are then transferred into a water bath at 35°C and stirred for 2 h. Next, 400 mL deionized water is gradually added in the pre-oxidized graphite and stirred for 2 h. The temperature is raised to 95°C for 4 min. Meanwhile, the diluted mixture turned brown. After then, 12 mL H_2O_2 (30%) is slowly added to remove the excess MnO_4^- , and the mixture is washed with 1 mol/L until all impurity ions are completely removed. Finally, the product is washed with deionized water until the pH reaches neutral. The washed product is later centrifuged at 10000rpm for 20min to obtain GO.

Preparation of conductive wood. 3 cm thick flat sawn boards are conditioned to 10% moisture content (MC) in an oven (DZF-6210, Shanghai, China). They are later cut into suitable experimental samples using an electric circular saw into dimension of $R^*T^*L=30\text{ mm}\times 30\text{ mm}\times 10\text{ mm}$. The end-matched sample is selected and treated by circulating boiling, steaming, and freezing in deionized water until the color of the solution turned clear. Next, the samples are dried at 105 °C until the moisture content reaches 10% MC. Then, the samples are impregnated in certain GO concentration and they are later treated using a pulsed vacuum process. And then, the products are washed several times with deionized water until small amount of residual GO remained on the surface. The products are dried again at 60 °C for 24 h. Subsequently, the products with GO are impregnated with ascorbic acid solution (AA) using a second pulse vacuum process. After which, the samples are put in pressurized sterilization pot (LDZX-50KBS, China) at 100°C for 2h in order to accelerate the reduction of GO. Finally, the products are dried at 60 °C for 24 h to reach a MC of 10% and they are stored for the following experiments. The synthesis processes of conductive wood samples are described in **Figure. 1**.

Characterization

Conductivity and Distribution of Resistivity. The surface resistivity and volume resistivity of the sample are evaluated using a volume surface resistivity tester (BEST 121, China) according to the Chinese national military standard GJB2604-96[35]. The distribution of resistivity is measured using a four-stage probe tester (RTS-9, China).

Mercury Intrusion Porosimetry. The pore size distribution and porosity of sample are determined using an automated mercury porosimeter (Autopore TM IV 9500, Norcross, GA, USA). The pore distribution is determined with the Washburn equation.

Nitrogen Adsorption. In order to understand the changes in the mesoporous structure of the conductive wood, the specific surface area (SSA) of wood is determined based on N₂ adsorption at its boiling point (77K). The Brunauer-Emmett-Teller (BET) surface area (SBET) of the sample is evaluated using an accelerated surface area (Brunauer, Emmett, & Teller, 1938). The pore-size distribution is calculated using the Barrett-Joyner-Halenda (BJH) method (Barrett, Joyner, & Halenda, 1951). The dimension of the sample used for nitrogen adsorption measurement is $R^*T^*L=1\text{ mm}\times 1\text{ mm}\times 5\text{ mm}$.

SEM Analysis. Test sample ($R^*T^*L=5\text{ mm}\times 5\text{ mm}\times 0.5\text{ mm}$) is sliced from the natural wood and conductive wood using a microtome (REM-700, Yamato). Field Emission Scanning Electron Microscope (FESEM, GAIA 3 XMN, TESCAN) is used to observe the morphologies of the surfaces with the magnification of up to 10,000 times. The EDS mapping mode is used to analyze the element distribution.

XPS Analysis. XPS spectra are recorded using a X-Ray Photoelectron Spectrometer (Escalab 250Xi, Thermo Fisher, USA) with an Al K α x-ray source, at a pass energy of 1 eV for survey scans and 0.05 eV for high-resolution scans. The required sample size is $R^*T^*L=10\text{ mm}\times 10\text{ mm}\times 2\text{ mm}$.

FTIR Analysis. FTIR spectra are recorded using a spectrophotometer (TENSOR II 03040404, BRUKER, Germany). Wood samples are grinded into uniform size mesh sizes (200 mesh). Each sample together with KBr is pressed to form a pallet before detection. FTIR spectra are obtained between 400 and 4000 cm^{-1} with 32 scans as the absorbance mode for the spectrum.

XRD Analysis. XRD patterns are obtained on a Bruker powder X-ray diffractometer (Advance D8 Bruker, Germany) operated at 40 kV and 40 mA using Cu-K α radiation ($\lambda=1.54$ nm) with 500 mg of each specimen sample. The data is collected within a 2θ scanning range of 10-80°.

CRM Analysis. The distribution of rGO in conductive wood is tested using a Laser Confocal Raman Microspectroscopy (Qontor, Renishaw, UK). A laser in the visible wavelength range ($\lambda= 532$ nm) is used. 50 times magnification is used, and the laser power is at 1%. Testing is conducted using the multi-point area scanning static method (center point is 1500 cm^{-1}).

Thermogravimetric Analysis. Thermogravimetric curve (TG) and differential scanning calorimetry (DSC) analysis are performed in an argon atmosphere with a 10 °C/min heating rate (STA449C, Netzsch, Germany). The dimension of the sample used is $R*T*L=2$ mm \times 2 mm \times 5 mm.

Holzer Effect Tester. Although the resistance instrument can reflect the electrical conductivity of impregnated wood samples, conducting a Holzer effect tester (Lake Shore 7707, USA) can validate the accuracy of its displaying resistivity. It also measures the carrier concentration per unit area, electron mobility, and conductivity type of materials by passing currents in 3-D directions. Finally, the hall coefficient of Holzer electric field comes out by imposing electromagnetic field, which can produce an additional transverse electric field- Holzer electric field.

Digital DC regulated power supply. In order to verify the conductive effect in 3D direction of conductive wood, a one-dimensional closed-loop circuit is established, which included a conductive wood, a diode, a digital DC regulated power (RPS3003D-2, China), a LED bulb. When the voltage was adjusted, a current regulation value on the instrument panel was displayed as 0.00apm, the current is a default value 3.00 amp.

Declarations

Acknowledgements

This work was supported by the National Natural Science Foundation of China (31760186); Inner Mongolia Natural Science Foundation of China (2019LH03025); the High-Level Talent Research Initiation Project of Inner Mongolia Agricultural University (NDYB2018-59); Science and Technology Achievements Transformation Project of Inner Mongolia Autonomous Region in China (CGZH2018136); National Key R&D Projects for the 13th Five-Year Plan (2017YFD0600202); "Grass Talents" Engineering Youth Innovation and Entrepreneurship of Inner Mongolia Autonomous Region in China (Q2017053).

Author Contributions

The manuscript was written through contributions of all authors. All authors have given approval to the final version of the manuscript. † Li Wang, Xiao T. Zhang, and Xi M. Wang contributed equally to this paper.

Li Wang: Methodology, Investigation, Writing-Original draft preparation. **Xiao T. Zhang:** Conceptualization, Methodology, Writing-Review & Editing. **Jian F. Yu:** Conceptualization, Writing-Review & Editing, Supervision, Project administration. **Xi M. Wang:** Software Programming, Validation Verification, Formal analysis. **Yu K. Ren:** Formal analysis, Resources, Writing-Original Draft. **Sun G. Wang:** Formal analysis, Investigation Conducting, Resources. **Zhe Wang:** Software Programming, Formal analysis. **Li L. Li:** Software Programming, Formal analysis. **Zhang J. Chen:** Investigation Conducting, Resources. **Qin He:** Formal analysis, Investigation Conducting. **Lihong Yao:** Investigation Conducting, Resources. **Yi N. Hao:** Formal analysis, Resources. **Li J. Ding:** Formal analysis, Investigation Conducting, Resources. **Qi Li:** Investigation Conducting, Resources. **Hua Q. Duo:** Conceptualization, Methodology. **WHITE Marshall:** Investigation Conducting, Resources.

Competing interest

The authors declare no competing interests.

References

- [1] Kuqo, A., Mai, C. Mechanical properties of lightweight gypsum composites comprised of seagrass *Posidonia oceanica* and pine (*Pinus sylvestris*) wood fibers. *Construction and Building Materials*. **282**, 122714 (2021). <https://doi.org/10.1016/j.conbuildmat.2021.122714>.
- [2] Ramage, M. H. et al. The wood from the trees: The use of timber in construction. *Renew Sustain Energy Rev*. **68**, 333-359(2017). <https://doi.org/10.1016/j.rser.2016.09.107>.
- [3] H. Y. Zhou. et al. Conductive and fire-retardant wood/polyethylene composites based on a continuous honeycomb-like nanoscale carbon black network. *Construction and Building Materials*. **233**, 117369(2020). <https://doi.org/10.1016/j.biombioe.2018.03.007>.
- [4] J. Y. Wan. et al. Highly Anisotropic Conductors. *Adv. Mater*. **29**, 1703331(2017). <https://doi.org/10.1002/adma.201703331>
- [5] Berglund, L. A., Burgert, I. Bioinspired Wood Nanotechnology for Functional Materials. *Adv. Mater*. **30**, 1704285(2018). <https://doi.org/10.1002/adma.201704285>.
- [6] Łukawski, D., Dudkowiak, A., Janczak, D., Lekawa-Raus, A. Preparation and applications of electrically conductive wood layered composites. *Composites Part A: Applied Science and Manufacturing*. **27**, 105656(2019). <https://doi.org/10.1016/j.compositesa.2019.105656>.

- [7] Xu, H., Li Y., Han, X. S., Cai, H. Z., Gao, F. Carbon black enhanced wood-plastic composites for high-performance electromagnetic interference shielding. *Materials Letters*. **285**, 129077(2021). <https://doi.org/10.1016/j.matlet.2020.129077>.
- [8] Zhu, S. et al. Multi-functional and highly conductive textiles with ultra-high durability through 'green' fabrication process. *Chemical Engineering Journal*. **406**, 127140(2021). <https://doi.org/10.1016/j.cej.2020.127140>.
- [9] Xiong, C. Y. et al. Carbonized wood cell chamber-reduced graphene oxide@PVA flexible conductive material for supercapacitor, strain sensing and moisture-electric generation applications. *Chemical Engineering Journal*. **418**, 129518(2021). <https://doi.org/10.1016/j.cej.2021.129518>.
- [10] Han, X. et al. Tour, Laser-Induced Graphene from Wood Impregnated with Metal Salts and Use in Electrocatalysis. *ACS Appl. Nano Mater.* **1**, 5053(2018). <https://doi.org/10.1021/acsanm.8b01163>.
- [11] Zhang, W. Y. et al. Graphene-quantum-dots-induced MnO₂ with needle-like nanostructure grown on carbonized wood as advanced electrode for supercapacitors. *Carbon*. **162**, 114-123(2020). <https://doi.org/10.1016/j.carbon.2020.02.039>.
- [12] Wang, X. C., Zhao, J., Cui, E. Z., Sun, Z. F., Yu, H. Nano/microstructures and mechanical properties of Al₂O₃-WC-TiC ceramic composites incorporating graphene with different sizes. *Materials Science and Engineering: A*. **812**, 141132(2021). <https://doi.org/10.1016/j.msea.2021.141132>.
- [13] Wu, C. L. et al. Carbon nanotubes grown on the inner wall of carbonized wood tracheids for high-performance supercapacitors. *Carbon*. **150**, 311-318(2019). <https://doi.org/10.1016/j.carbon.2019.05.032>.
- [14] Zhang, S. et al. High performance flexible supercapacitors based on porous wood carbon slices derived from Chinese fir wood scraps. *Journal of Power Sources*. **424**, 1-7(2019). <https://doi.org/10.1016/j.jpowsour.2019.03.100>.
- [15] Pikul, J. H. et al. High strength metallic wood from nanostructured nickel inverse opal materials. *Sci. Rep.* **9**, 1-12(2019). <https://doi.org/10.1038/s41598-018-36901-3>.
- [16] Dong, B. et al. Multiple methods for the identification of heavy metal sources in cropland soils from a resource-based region. *Sci. Total Environ.* **651**, 3127-3138(2019). <https://doi.org/10.1016/j.scitotenv.2018.10.130>.
- [17] Robey, N. M., Solo-Gabriele, H. M., Jones, A. S., Marini J., Townsend, T. G. Metals content of recycled construction and demolition wood before and after implementation of best management practices. *Environ. Pollut.* **242**, 1198-1205(2018). <https://doi.org/10.1016/j.envpol.2018.07.134>.

- [18] Lee, W. S. V., Leng, M., Li, M., Huang, X. L., Xue, J. M. Sulphur-functionalized graphene towards high performance supercapacitor. *Nano Energy*. **12**, 250-257(2015).
<https://doi.org/10.1016/j.nanoen.2014.12.030>.
- [19] Ochapski, M. W., Ataç, D., Sanderink, J. G. M., Kovalgin, A. Y., de Jong, M. P. Li intercalation into multilayer graphene with controlled defect densities. *Carbon Trends*. **4**, 100045(2021).
<https://doi.org/10.1016/j.cartre.2021.100045>.
- [20] Song, X. X. et al. Formaldehyde adsorption effects of chlorine adatoms on lithium-decorated graphene: A DFT study. *Chemical Physics Letters*. 761, 138085(2020).
<https://doi.org/10.1016/j.cplett.2020.138085>.
- [21] Foo, M. E., Gopinath, S. C. B. Feasibility of graphene in biomedical applications. *Biom. Pharm.* **94**, 354-361(2017). <https://doi.org/10.1016/j.biopha.2017.07.122>.
- [22] Bhagat, A., Mullen, K. Pseudo-magnetic quantum Hall effect in oscillating graphene. *Solid State Commun.* **287**, 31-34(2019). <https://doi.org/10.1016/j.ssc.2018.09.017>.
- [23] Sinclair, R. C., Suter, J. L., Coveney, P. V. Graphene-Graphene Interactions: Friction, Superlubricity, and Exfoliation. *Adv. Mater.* **30**, 1705791(2018). <https://doi.org/10.1002/adma.201705791>.
- [24] Mkhoyan, K. A. et al. Atomic and Electronic Structure of Graphene-Oxide. *Nano Lett.* **9**, 1058-1063(2010). <https://doi.org/10.1021/nl8034256>.
- [25] Petukhov, D. I., Kapitanova, O. O., Eremina, E. A., Goodilin, E. A. Preparation, chemical features, structure and applications of membrane materials based on graphene oxide. *Mendeleev Communications*. **31**, 137-148(2021). <https://doi.org/10.1016/j.mencom.2021.03.001>.
- [26] Huang, X. Y. et al. Thermal conductivity of graphene-based polymer nanocomposites. *Materials Science and Engineering: R: Reports*. **142**, 100577(2020). <https://doi.org/10.1016/j.mser.2020.100577>.
- [27] Wang, C. L. et al. Boosting oxygen evolution reaction on graphene through engineering electronic structure. *Carbon*. **170**, 414-420(2020). <https://doi.org/10.1016/j.carbon.2020.08.041>.
- [28] Xu, Y. L. et al. Lightweight microwire/graphene/silicone rubber composites for efficient electromagnetic interference shielding and low microwave reflectivity. *Composites Science and Technology*. **189**, 108022(2020). <https://doi.org/10.1016/j.compscitech.2020.108022>.
- [29] Nan, B. F. et al. A multifunctional thermal management paper based on functionalized graphene oxide nanosheets decorated with nanodiamond. *Carbon*. **161**, 132-145(2020). <https://doi.org/10.1016/j.carbon.2020.01.056>.
- [30] Wu, Y. P. et al. Two-dimensional black phosphorus: Properties, fabrication and application for flexible supercapacitors. *Chemical Engineering Journal*. **41**, 128744(2021).

<https://doi.org/10.1016/j.cej.2021.128744>.

[31] Zhi, D. D., Li, T., Li, J. Z., Ren, H. S., Meng, F. B. A review of three-dimensional graphene-based aerogels: Synthesis, structure and application for microwave absorption. *Composites Part B: Engineering*. 211, 108642(2021) <https://doi.org/10.1016/j.compositesb.2021.108642>.

[32] Worsley, M. A. et al. Synthesis of Graphene Aerogel with High Electrical Conductivity. *J. Am. Chem. Soc.* **132**, 14067-14069(2010). <https://doi.org/10.1021/ja1072299>

[33] Li, J. X. et al. Hierarchical nanoporous microtubes for high-speed catalytic microengines. *NPG Asia Materials*. **7**, e94(2015). <https://doi.org/10.1038/am.2014.11>

[34] Marinho, Ghislandi, Tkalya, B. M. E., Koning, C. E., de With, G. Electrical conductivity of compacts of graphene, multi-wall carbon nanotubes, carbon black, and graphite powder. *Powder Technol.* **221**, 351-358(2012). <https://doi.org/10.1016/j.powtec.2012.01.024>

[35] Li, J. P. et al. General Specification for Military Electromagnetic Shielding Coatings. *National military standards of China*, GJB **1996**.

[36] Rosenholm, J. B. Critical evaluation of models for self-assembly of short and medium chain-length surfactants in aqueous solutions. *Advances in Colloid and Interface Science*. **276**, 102047(2020). <https://doi.org/10.1016/j.cis.2019.102047>.

[37] Meng, X. Using cellulose nanocrystals for graphene/hexagonal boron nitride nanosheet films towards efficient thermal management with tunable electrical conductivity. *Composites Part A: Applied Science and Manufacturing*. **138**, 106089(2020). <https://doi.org/10.1016/j.compositesa.2020.106089>.

[38] Zhang, K. T., Ketterle, L., Järvinen, T., Lorite, G. S., Hong, S. Henriikki Liimatainen, Self-assembly of graphene oxide and cellulose nanocrystals into continuous filament via interfacial nanoparticle complexation. *Materials & Design*. **193**, 108791(2020). <https://doi.org/10.1016/j.matdes.2020.108791>.

[39] Qin, D. D. et al. Ultra-high gas barrier and enhanced mechanical properties of corn cellulose nanocomposite films filled with graphene oxide nanosheets. *Carbohydrate Polymer Technologies and Applications*. **2**, 100066(2021). <https://doi.org/10.1016/j.carpta.2021.100066>.

[40] Croitoru, C. et al. Surface properties of thermally treated composite wood panels. *Appl. Surf. Sci.* **438**, 114-126(2018). <https://doi.org/10.1016/j.apsusc.2017.08.193>.

[41] Song, J. W. et al. Processing bulk natural wood into a high-performance structural material. *Nature*. **554**, 224-228(2018). <https://doi.org/10.1038/nature25476>

[42] Nypelö, T., Berke, B., Spirk, S., Sirviö, J. A. Review: Periodate oxidation of wood polysaccharides—Modulation of hierarchies. *Carbohydrate Polymers*. 252, 117105(2021). <https://doi.org/10.1016/j.carbpol.2020.117105>.

- [43] Alharbi, T. M. D. et al. Shear stress mediated scrolling of graphene oxide. *Carbon*. 137, 419-424(2018). <https://doi.org/10.1016/j.carbon.2018.05.040>
- [44] Ma, L. Y., Li, J. N., Ma, X. J. Improvement of electrochemical properties of activated carbon hollow fibers from liquefied wood by charcoal power. *Materials Letters*. **255**, 126544(2019). <https://doi.org/10.1016/j.matlet.2019.126544>.
- [45] Nebol'sin, V. Galstyan, A. V., Silina, Y. E. Graphene oxide and its chemical nature: Multi-stage interactions between the oxygen and graphene. *Surfaces and Interfaces*. **21**, 100763(2020). <https://doi.org/10.1016/j.surfin.2020.100763>.
- [46] Gao, Z. P., Li, Zhang, Z. D. W. Three-dimensional quantum Hall effect in Weyl and double-Weyl semimetals. *Phys. Lett. A*. **382**, 3205(2018). <https://doi.org/10.1016/j.physleta.2018.08.022>
- [47] B. C. Ozkan, T. Soganci, H. Turhan, M. Ak, Investigation of rGO and chitosan effects on optical and electrical properties of the conductive polymers for advanced applications. *Electrochim. Acta*. 2018, **295**, 1044-1071. <https://doi.org/10.1016/j.electacta.2018.11.032>
- [48] Chau, T. K., Suh, Kang, D. H. Detection of hidden localized states by the quantum Hall effect in graphene. *Current Applied Physics*. **23**, 26-29(2021). <https://doi.org/10.1016/j.cap.2020.12.016>.
- [49] Mohammadi, Y. Integer quantum Hall effect in AAA-stacked trilayer graphene. *Physica B: Condensed Matter*. **613**, 413022(2021). <https://doi.org/10.1016/j.physb.2021.413022>.
- [50] Yang, Z. J. et al. Energetic nanoarray structures by confined crystallization for enhanced energy-release efficiency. *Chemical Engineering Journal*. **403**, 126408(2021). <https://doi.org/10.1016/j.cej.2020.126408>.
- [51] Xie, L. Recent progress of organic photovoltaics for indoor energy harvesting. *Nano Energy*. **82**, 105770(2021). <https://doi.org/10.1016/j.nanoen.2021.105770>.
- [52] Mishra, S., Acharya, R. Photocatalytic applications of graphene based semiconductor composites: A review, *Materials Today: Proceedings*. **35**, 164-169(2021). <https://doi.org/10.1016/j.matpr.2020.04.066>.

Figures

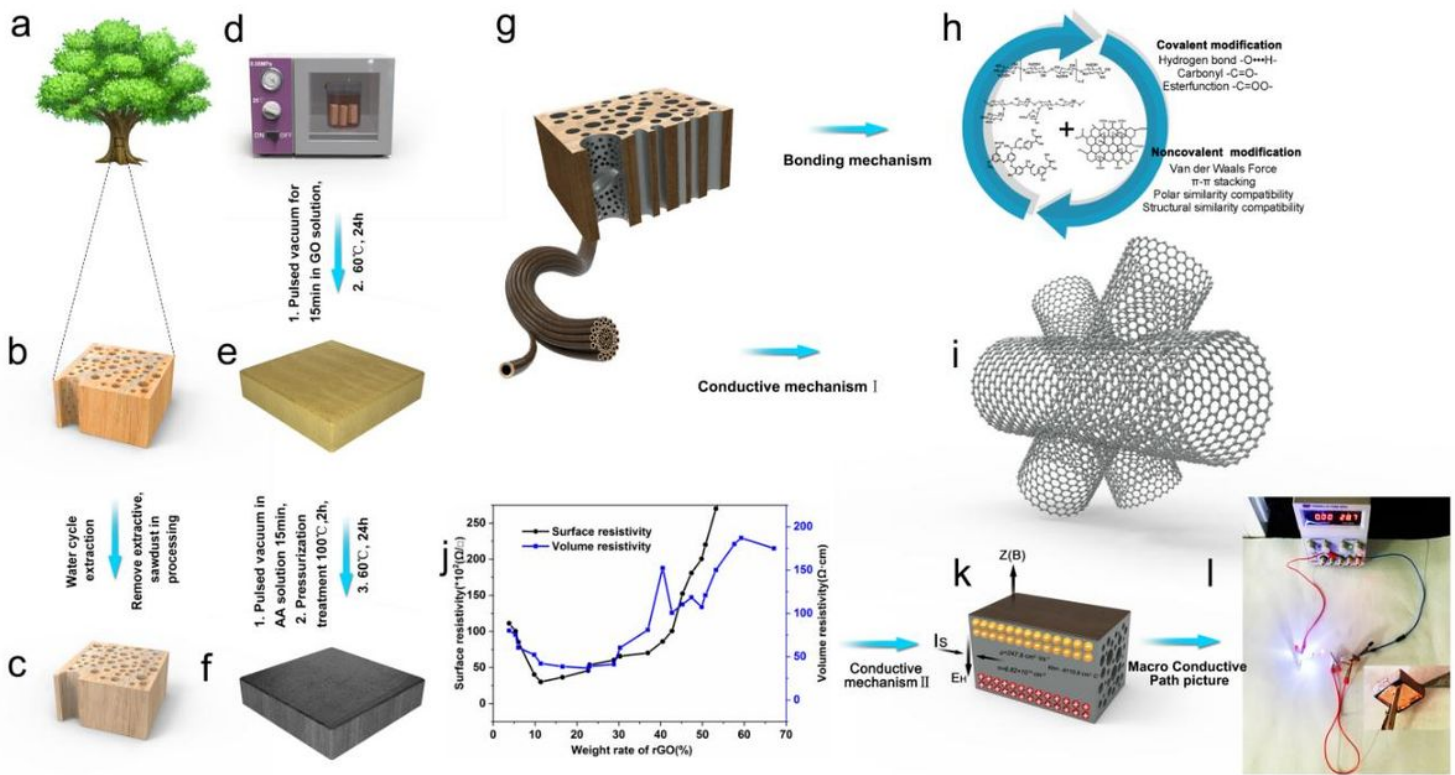


Figure 1

Schematic to display the synthesis process of conductive wood and conductive-bonding mechanism. a-b, Schematic of wood cut from poplar tree. c, Sample treated by circulating water. d, Composition of sapwood and GO by pulsed vacuum for 15min and dried at 60 oC for 24h. e, Wood-based graphene oxide composites. f, Conductive wood in which GO is reduced by AA. g, Aligned structure of conductive wood. h, Bonding mechanism of wood and rGO. i, Three-dimensional anisotropic conductive structure and constructed conductive path in conductive wood caused by the pore structure of wood with multiple connectivity. j, Percolation threshold of rGO in conductive wood. k, Conduction with superior mobility in closely galvanic circle and hall effect formed. l, Picture to show wood-graphene becomes highly conductive after synthesis procedure.

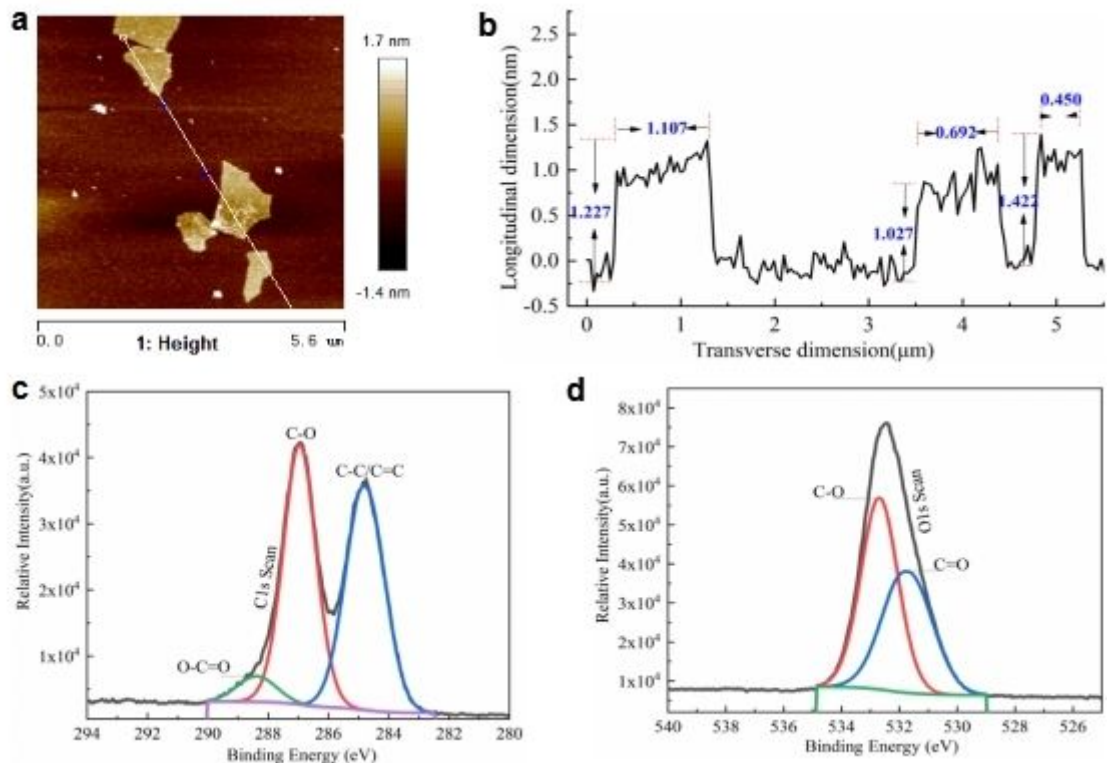


Figure 2

Characterization of synthesized GO as conductive filler in the wood matrix. a, AFM topographic map of GO. b, Height profile of GO. c, High-resolution C1s XPS of GO. d, High-resolution O1s of GO.

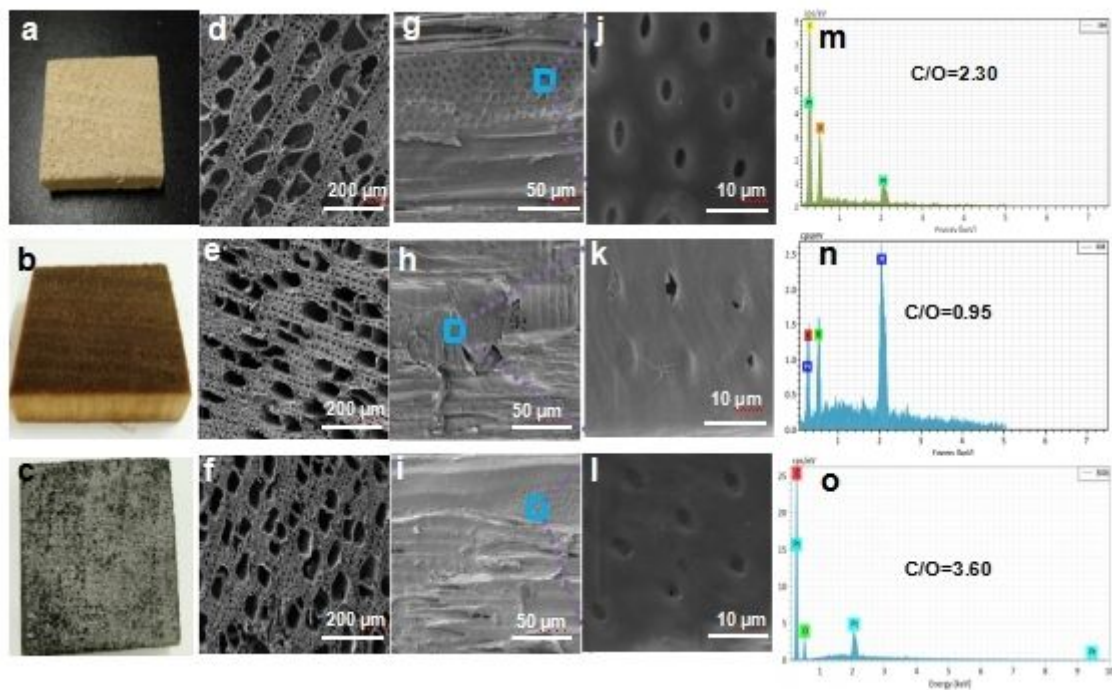


Figure 3

SEM and EDS analysis of natural wood and conductive wood. a, Photograph of natural wood. b, Photograph of GO/wood composite. c, Photograph of rGO/wood (conductive wood). d, SEM image of

natural wood in the cross-section orientation. e, SEM image of GO/wood composite in the cross-section orientation. f, SEM image of conductive wood in the cross-section orientation. g, SEM image of natural wood in the radial-section orientation. h, SEM image of GO/wood composite in the radial-section orientation. i, SEM image of conductive wood in the radial-section orientation. j, Magnified SEM image of natural wood in the radial-section orientation. k, Magnified SEM image of GO/wood composites in the radial-section orientation. l, Magnified SEM image of conductive wood in the radial-section orientation. m, EDS analysis of natural wood. n, EDS analysis of GO/wood composites. o, EDS analysis of conductive wood.

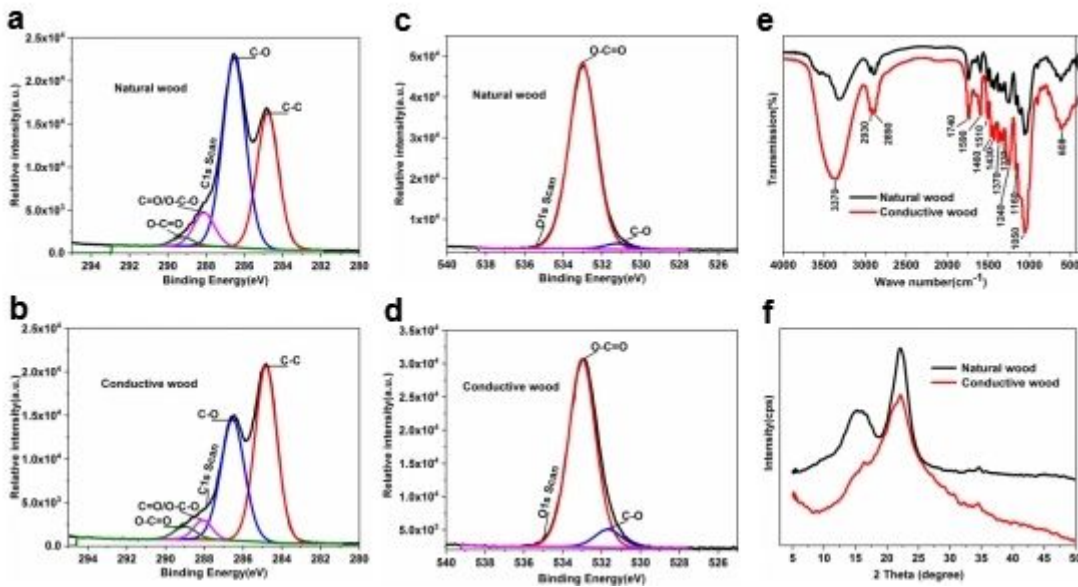


Figure 4

Characterization of natural wood and conductive wood. a, C1s XPS spectrum of natural wood. b, C1s XPS spectrum of conductive wood. c, O1s XPS spectrum of natural wood. d, O1s XPS spectrum of conductive wood. e, FTIR spectra of natural wood and conductive wood. f, XRD spectra of natural wood and conductive wood.

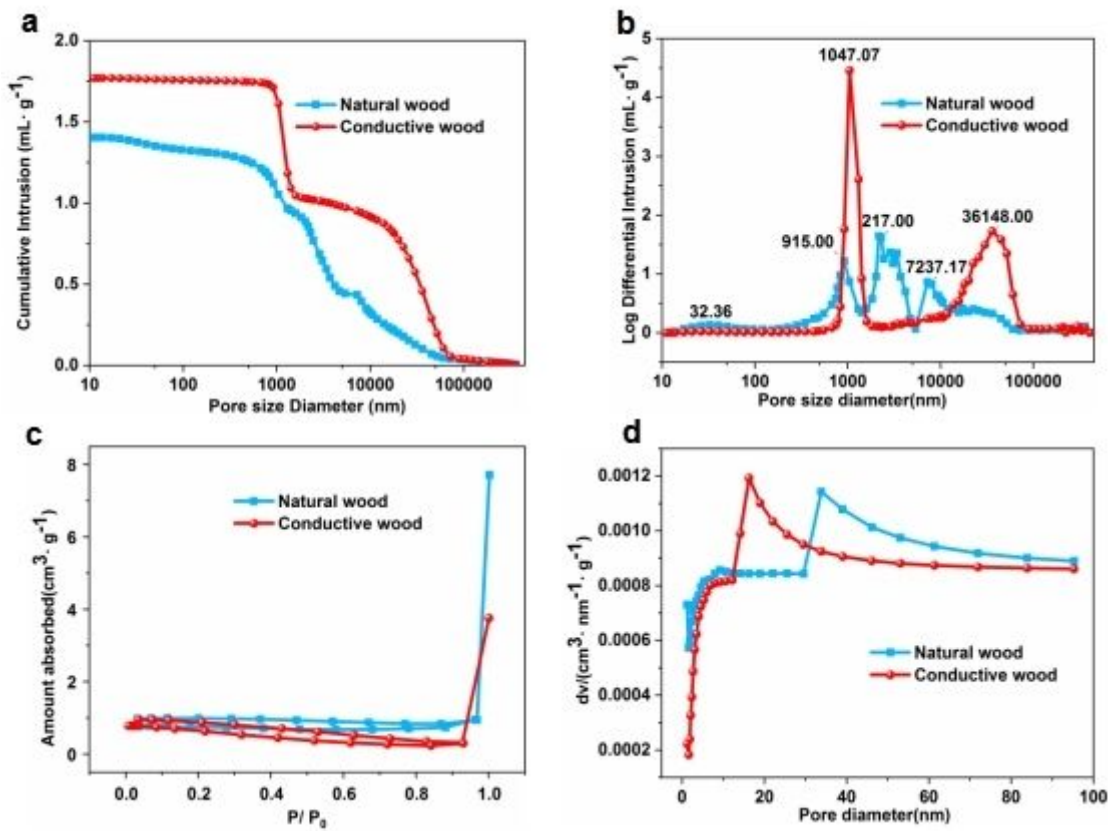


Figure 5

Pore structure of natural wood and conductive wood. a, Mercury intrusion method. b, Effects of pore diameter on cumulative intrusion. c, N₂ adsorption/desorption curves of natural wood and conductive wood. d, Pore size distribution of natural wood and conductive wood.

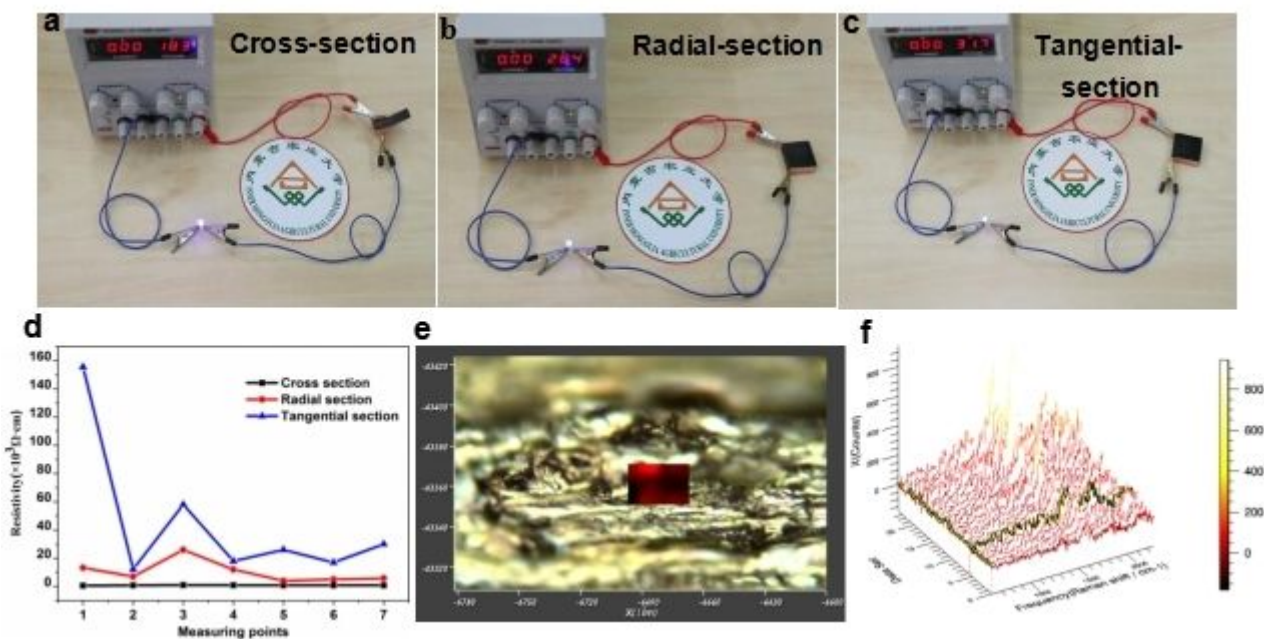


Figure 6

Three-dimensional anisotropic electrical conductivity mechanism of conductive wood. a-c, Macroscopic conductive path pictures of cross-section (a), radial-section (b), and tangential-section (c), respectively. d, Resistivity measurement of conductive wood in three various orientations (cross-section, radial-section and tangential-section). e, Intensity distribution of "G" peak on area scan of conductive wood of CRM. f, Multipoint spectrum on area scan of conductive wood of CRM.

Supplementary Files

This is a list of supplementary files associated with this preprint. Click to download.

- [20210608Supportinginformation.docx](#)